

RESEARCH ARTICLE

10.1002/2016JD025962

Key Points:

- An empirical method is developed to track the spatial and temporal evolutions of the Pacific Decadal Precession (PDP)
- An approximation to this method is developed to provide real-time monitoring of the PDP
- Application of the method to ocean-atmosphere models can assess whether they properly reproduce the observed PDP's characteristic evolution

Correspondence to:

B. T. Anderson,
brucea@bu.edu

Citation:

Anderson, B. T., J. C. Furtado, E. Di Lorenzo, and D. J. Short Gianotti (2017), Tracking the Pacific Decadal Precession, *J. Geophys. Res. Atmos.*, 122, 3214–3227, doi:10.1002/2016JD025962.

Received 21 SEP 2016

Accepted 19 FEB 2017

Accepted article online 22 FEB 2017

Published online 20 MAR 2017

Tracking the Pacific Decadal Precession

Bruce T. Anderson¹ , Jason C. Furtado² , Emanuele Di Lorenzo³ , and Daniel J. Short Gianotti⁴

¹Department of Earth and Environment, Boston University, Boston, Massachusetts, USA, ²School of Meteorology, University of Oklahoma, Norman, Oklahoma, USA, ³School of Earth and Atmospheric Science, Georgia Institute of Technology, Atlanta, Georgia, USA, ⁴Parsons Laboratory, Massachusetts Institute of Technology, Cambridge, Massachusetts, USA

Abstract Events of recent years—including extended droughts across California, record fires across western Canada, and destabilization of marine ecosystems—highlight the profound impact of multiannual to decadal-scale climate shifts upon physical, biological, and socioeconomic systems. While previous research has focused on the influence of decadal-scale climate oscillations such as the Atlantic Multidecadal Oscillation and the Pacific Decadal Oscillation/Interdecadal Pacific Oscillation, recent research has revealed the presence of a quasi-decadal mode of climate variability that, unlike the quasi-stationary standing wave-like structure of the oscillatory modes, involves a progression of atmospheric pressure anomalies around the North Pacific, which has been termed the Pacific Decadal Precession (PDP). In this paper we develop a set of methods to track the spatial and temporal evolutions of the PDP within historical observations as well as numerical model simulations. In addition, we provide a method that approximates the time evolution of the PDP across the full period of available data for real-time monitoring of the PDP. Through the development of these tracking methods, we hope to provide the community with a consistent framework for future analysis and diagnosis of the PDP's characteristics and underlying processes, thereby avoiding the use of different, and disparate, phenomenological- and mathematical-based indices that can confound our understanding of the PDP and its evolution.

1. Introduction

A substantial amount of research has focused on the impacts of human-induced global warming upon natural and human systems, both historically and over the next century [e.g., *Walther et al.*, 2002; *Dell et al.*, 2008; *Mendelsohn and Dinar*, 2009; *Gosling et al.*, 2009; *Schlenker et al.*, 2011; *Doney et al.*, 2012; *Moritz and Agudo*, 2013; *Benmarhnia et al.*, 2014]. However, climate variations, particularly at the regional level, of equal or greater magnitude can occur over just 5–10 years in response to decadal-scale climate oscillations [*Solomon et al.*, 2011], such as the Atlantic Multidecadal Oscillation [*Enfield et al.*, 2001], the Pacific Decadal Oscillation (PDO) [*Mantua et al.*, 1997], and the North Pacific Gyre Oscillation [*Di Lorenzo et al.*, 2008].

Recently, a new mode of quasi-decadal variability—termed the Pacific Decadal Precession (PDP)—has been revealed through both empirical and statistical analyses of meteorological and dynamical fields across the tropical and extratropical North Pacific [*Anderson et al.*, 2016a, 2016b]. As with other modes of low-frequency variability, the PDP is accompanied by persistent, multiyear shifts in atmospheric circulations and concomitant changes to regional climates that provide an explanation for many climate disturbances that have influenced the North Pacific/North American sector both historically and over the last few years. However, unlike other low-frequency oscillatory modes of variability—which tend to be characterized by quasi-stationary, standing wave-like patterns—the PDP is characterized by a slow (~10 year) progression of atmospheric pressure variations around the North Pacific basin, which makes tracking its spatial and temporal evolutions more difficult.

That said, the climate community has developed a repertoire of methods for tracking propagating, wave-like features in the atmosphere, in particular, those associated with intraseasonal shifts in convective activity across the tropical Indian and Pacific Oceans that accompany the Madden-Julian Oscillation (MJO) [*Madden and Julian*, 1971; *Zhang*, 2005]. Unfortunately, the development of multiple indices for tracking the MJO's evolution has, in some cases, confounded the community's ability to analyze and diagnose the underlying phenomena and processes in a consistent framework [*Kiladis et al.*, 2014]. As such, here we start by developing and proposing a common method for tracking the PDP within a given spatiotemporal data set such that subsequent analysis and diagnosis of the characteristics of the PDP within and across data sets can

be performed by using a standardized procedure. In this way we hope to facilitate a more rapid understanding of its behavior, leading to improved forecasts of its evolution and societal impacts.

The paper itself is laid out as follows. In section 2 we detail the data used in the analysis, as well as the methods for analyzing these data. In section 3 we develop a method for tracking the state of the observed PDP within retrospective reanalyses. In this section we also provide a modification of this method such that it can be used for real-time monitoring of the PDP within more up-to-date reanalyses. Finally, we apply the method to independent data taken from long integrations of a coupled ocean-atmosphere climate model as a way to evaluate the characteristics of the simulated PDP against those found in observations. Sections 4 and 5 then discuss and summarize the results of this research effort.

2. Data and Methods

2.1. Data

For this study, observationally based data are taken from the 20th Century Reanalysis version 2 (20CRv2) [Compo *et al.*, 2011]. These data span the period of 1871–2012 and consist of monthly mean values on a $2^\circ \times 2^\circ$ longitude/latitude grid and on 24 pressure levels ranging nonuniformly from 1000 to 10 hPa. For our analysis we confine our investigation to 850 hPa geopotential height anomalies, derived by removing from the monthly values the long-term climatological mean for that month. Additionally, we confine our analysis to anomalous values during the extended boreal winter (November–March). Since our interest is in isolating the known quasi-decadal structure over the North Pacific basin, except where noted, we apply a $7\text{--}20\text{ year}^{-1}$ Butterworth band-pass filter to the data prior to performing any analytical methods (described below); for ease throughout the manuscript we will refer to variations in the band-pass filtered data as “low-frequency” variations. To extend the observationally based data up to the (near) present, we will also analyze 850 hPa geopotential height fields taken from the National Centers for Environmental Prediction (NCEP)/National Center for Atmospheric Research (NCAR) Reanalysis 1 (R-1) [Kalnay *et al.*, 1996], which are available on a 2.5° longitude/latitude grid and at monthly time resolution from 1948 to 2015. In addition to the observationally based data, to test the algorithms developed herein, we also conduct an analysis by using a 500 year preindustrial control run (i.e., greenhouse gas forcing is set to preindustrial levels) of the Community Climate System Model version 4 (CCSM4) (model specifications can be found in Gent *et al.* [2011]) used as part of the Coupled Model Intercomparison Project Phase 5 (CMIP5) [Taylor *et al.*, 2012]. As with the observationally based data, our interest is in the spatial and temporal evolution of the 850 hPa geopotential height fields, which are available on a $1.25^\circ \times 0.94^\circ$ longitude/latitude grid and at monthly time resolution.

2.2. Methods

2.2.1. Lagged Teleconnectivity Maps

As an initial stage of our analysis, we create lagged teleconnectivity maps of low-frequency variations in the 850 hPa geopotential height fields over the North Pacific ($15\text{--}80^\circ\text{N}$ and $125^\circ\text{E}\text{--}90^\circ\text{W}$) during extended boreal winter (November–March). These maps are similar to those described in Wallace and Gutzler [1981] and Nigam and Baxter [2015]. However, instead of basing the maps upon concurrent grid point regression values as in the earlier works, we base them upon lagged regression values so as to identify (potential) oscillating teleconnectivity patterns. Specifically, for each grid point in the domain of interest, we calculate the regression with all other grid points in the domain of interest for lags of 1–5 years. As with the standard teleconnectivity map analysis, for each grid point, we select the most negative regression value and assign its magnitude to represent the teleconnectivity value for that grid. For our analysis, there are five separate regression maps from which to select the teleconnectivity value for a given grid point, allowing us to identify local maxima in (negative) teleconnectivity at different lags, as opposed to prescribing the lag time a priori. These local maxima serve as base points, which can then be used to discern both the spatial and temporal structures of the accompanying teleconnection patterns. In principle, combinations of these base points can be used to create an index [e.g., Nigam and Baxter, 2015]. However, our interest here is simply to see whether the teleconnectivity maps, and accompanying base points, reveal any interesting characteristics of the patterns themselves. Hence, we will look at the concurrent and lagged regression maps associated with each base point separately.

2.2.2. Empirical Orthogonal Function Analysis and Extended EOF Analysis

As part of our analysis, we will also employ fairly standard statistical decomposition methods, namely, empirical orthogonal function (EOF) analysis (also referred to as principal component analysis or singular value decomposition) and extended EOF (EEOF) analysis. For the EOF analysis, the covariance matrix of low-frequency variations in the 850 hPa geopotential height fields over the North Pacific (15–80°N and 125°E–90°W) during extended boreal winter (November–March) is constructed, from which the eigenvectors and eigenvalues can be determined. For our purposes, EOF analysis will only be used to identify, and subsequently remove, signal related to the leading mode of low-frequency pressure variations over the central North Pacific that accompanies the PDO.

More pertinent to our need to identify and isolate (potential) modes of propagating teleconnections, we will employ an EEOF analysis [Weare and Nasstrom, 1982] which, like the lagged teleconnectivity maps, accounts for the covariance between time-lagged grid point anomalies explicitly. To do this, the spatiotemporal matrix of 7–20 year⁻¹ band-pass filtered 850 hPa geopotential height anomalies over the domain 15–80°N and 125°E–90°W during boreal winter (November–March) is extended by including (time) lagged values from 0 to 5 years (inclusive) at 1 year increments. Effectively, each of these time-lagged values is concatenated to the original spatiotemporal matrix as a separate set of maps, such that the time dimension is reduced by 5 years from T to T-5 but the spatial dimension is increased by a factor of 6 from N to 6 N, where T and N are the original size of the time and space dimensions, respectively.

As with the standard EOF analysis, the covariance matrix of the extended low-frequency variations in the 850 hPa geopotential height fields over the North Pacific is constructed, from which the eigenvectors and eigenvalues can be determined. Now however, the eigenvectors represent a series of six spatial patterns that contribute the most variance to the extended anomaly field, with the sequence of maps representing the progression of the anomalies over a 6 year period. For our purposes, we will refer to the third map as the “central” map, with the first two representing “lead” maps and the last three representing “lagged” maps. Further, the average projection of the maps onto the full field at various points in time (with the appropriate lead/lag time) defines the time evolution of the suite of spatial patterns that comprise the given mode of lagged (co)variability. Note that the time series for the propagating pattern of interest can also be obtained directly by applying a singular value decomposition to the extended spatiotemporal matrix directly.

Importantly, in EEOF analysis, eigenvalues will tend to form degenerate pairs. In this case, the two degenerate eigenvalues correspond to an oscillatory pair of eigenvectors that are time-lagged by a quarter phase (such that the spatial patterns at each common time lag remain orthogonal to one another, as do the two corresponding principal component time series). The presence of these EEOF pairs has been used previously to identify, and isolate, propagating intraseasonal features associated with the MJO [Roundy and Schreck, 2009]. Similarly here we will use pairs of EEOF eigenvalues to identify and isolate (potential) propagating, quasi-decadal features associated with the PDP.

3. Results

3.1. Observations

To start we examine the lagged teleconnectivity of low-frequency variations in the lower tropospheric (i.e., 850 hPa) height fields over the North Pacific (15–80°N and 125°E–90°W) during November–March (Figure 1). The analysis identifies one major teleconnectivity center over the Gulf of Alaska (A) and two minor teleconnectivity centers over the Bering Strait (B) and the Hawaiian Islands (Bb). To discern the lagged teleconnections associated with the major teleconnectivity center, the low-frequency variations of 850 hPa height anomalies at “A” are regressed against the concurrent and lagged 850 hPa anomalies across the rest of the domain (Figure 2). The concurrent anomalies (Figure 2a) indicate that the lagged teleconnectivity is initially associated with a prominent, basin-wide anomaly characteristic of variability in the Aleutian Low that accompanies the PDO [Mantua *et al.*, 1997]. As time progresses, the anomalies over the extratropical North Pacific decay and are eventually replaced by a similar monopole of opposite sign 5–6 years later, which tends to be shifted eastward of the initial anomalies (Figure 2f), resulting in a broad expanse of pressure anomalies off the coast of western North America, as noted by others [e.g., Wang *et al.*, 2009].

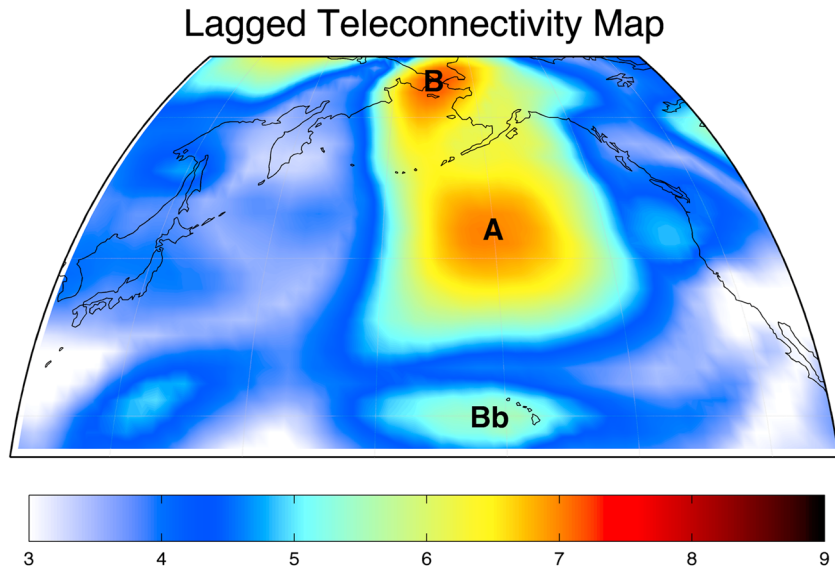


Figure 1. Lagged teleconnectivity map of 7–20 year⁻¹ band-pass filtered 850 hPa geopotential height anomalies for extended boreal winter (November–March) over the North Pacific (15–80°N and 125°E–90°W). Values designate the magnitude of the strongest negative regression between the given grid point and all other lagged (from 1 to 5 years inclusive) grid point values within the domain—see text for details. Regression values (m) are designated by the red/blue color bar at the bottom of the figure. The letters designate local centers of action for further analysis.

By contrast, the lagged teleconnections associated with the minor teleconnectivity centers comprise two base points of an evolving dipole pattern over the North Pacific (Figure 3). The 850 hPa height anomalies concurrent with low-frequency variations of 850 hPa height anomalies at both “B” and “Bb” (Figures 3a and 3g) indicate that the lagged teleconnectivity is initially associated with a north-south dipole characteristic of the North Pacific Oscillation/West Pacific pattern (NPO) [Walker and Bliss, 1932; Linkin and Nigam, 2008]. As time progresses, both lagged regression fields indicate the establishment of a pressure anomaly off the coast of western North America (Figures 3c and 3i). The lagged teleconnection associated with the northern pole of the NPO (B, Figure 3c) has a distinct zonal dipole structure with a corresponding pressure anomaly of opposite sign over the Bering Strait, while that associated with the southern pole (Bb, Figure 3i) tends to be followed by a single pressure center in the Gulf of Alaska. However, as time continues to progress, both eventually establish a north-south dipole of opposite sign ~5–6 years later (Figures 3f and 3l). Importantly, this progression, which is revealed from a relatively simple empirical analysis of the lagged teleconnectivity structure of the North Pacific pressure fields, is characteristic of the PDP [Anderson et al., 2016a, 2016b] and is what we want to represent with a single, robust index. The development of this index is the focus of the rest of the research.

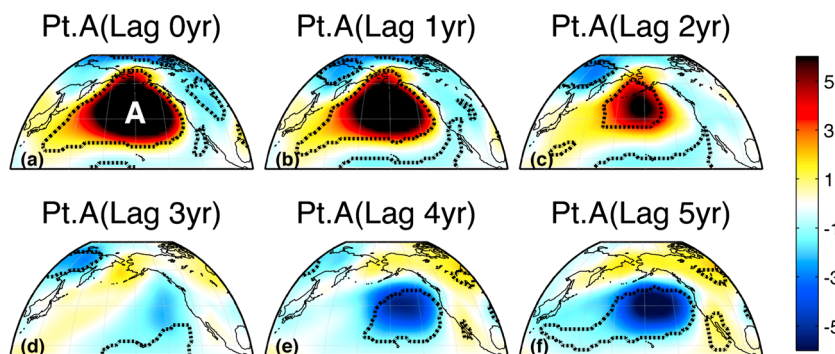


Figure 2. Lag regression of 7–20 year⁻¹ band-pass filtered extended boreal winter (November–March) 850 hPa geopotential height anomalies onto the local center of teleconnectivity action designated by (a) “A”. Regression values (m) are designated by the red/blue color bar at the right of the figure. The black contour designates the $p < 0.10$ value.

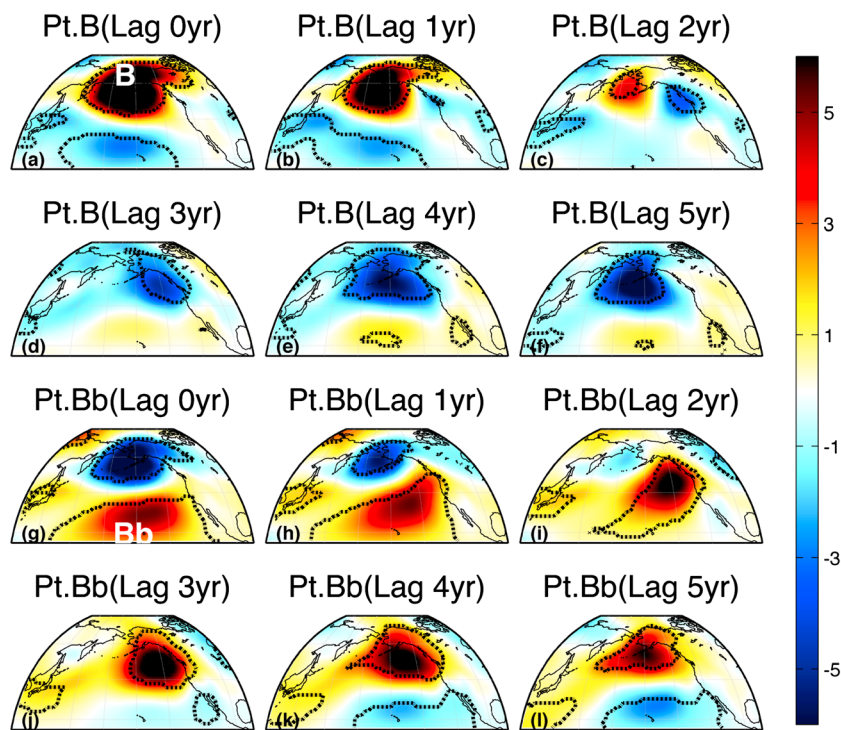


Figure 3. (a–f) Lag regression of $7\text{--}20\text{ year}^{-1}$ band-pass filtered extended boreal winter (November–March) 850 hPa geopotential height anomalies onto the local center of teleconnectivity action designated by (a) “B”. Regression values (m) are designated by the red/blue color bar at the right of the figure. The black contour designates the $p < 0.10$ value. (g–l) Same as Figures 3a–3f, except as regressed onto local center of teleconnectivity action, designated by “Bb” in Figure 3g.

Recognizing that we want to capture the PDP’s evolution within a broader spatiotemporal field, we turn to the EEOF analysis which, as noted earlier, is a standard method for obtaining a time series that tracks the MJO’s evolution [Roundy and Schreck, 2009]. As described above, here we apply the EEOF analysis to the spatiotemporal matrix of $7\text{--}20\text{ year}^{-1}$ band-pass filtered November–March 850 hPa geopotential height anomalies over the domain $15\text{--}80^\circ\text{N}$ and $125^\circ\text{E}\text{--}90^\circ\text{W}$ and time lagged from 0 to 5 years (inclusive) at 1 year increments. The resulting eigenvalues (Figure 4a) indicate two leading pairs of lagged variability. The first pair (represented by EEOF1 and EEOF2, Figures 4b and 4c) has a maximum time-lag correlation (at 3 years) of $r = 0.83$ and captures variability in the Aleutian Low that accompanies the PDO. During the “mature” phase of the PDO (Figure 4b), there is a prominent, basin-wide anomaly over the extratropical North Pacific, while during its “transition” phase (Figure 4c), anomalies are of the same sign/location but are less robust, similar to the transition phase of the related teleconnectivity maps (cf. Figure 2c).

By contrast, the second pair (represented by EEOF3 and EEOF4, Figures 4d and 4e) has a maximum time-lag correlation (at 2 years) of $r = 0.84$ and captures the zonal and meridional dipole structure of the PDP, respectively. In the zonal phase (Figure 4d), the pressure anomalies over the Aleutian Islands and off the coast of western North America are both prominent, as are the pressure anomalies over the Bering Strait and the central subtropical North Pacific in the meridional phase (Figure 4e). At the same time, both spatial patterns have substantial variations in the vicinity of the Aleutian Low, suggesting that some of the low-frequency variability in these regions may be influenced by the PDO.

To ensure that the PDP index we construct is not contaminated by the quasi-stationary variability that accompanies the PDO, we linearly remove via least squares regression signal related to the time series for the first EOF of the (nonextended) low-frequency pressure variations over the central North Pacific, which is characteristic of the PDO (not shown). We then repeat the EEOF analysis as above by using the residual 850 hPa geopotential height anomalies. The result is that the leading modes of lagged variability are now represented by zonal (EEOF1) and meridional (EEOF2) dipoles similar to those in Figures 4d and 4e, with a maximum time-lag correlation (at 3 years) of $r = 0.82$. In addition, the contemporaneous correlation between the EEOF1 (EEOF2)

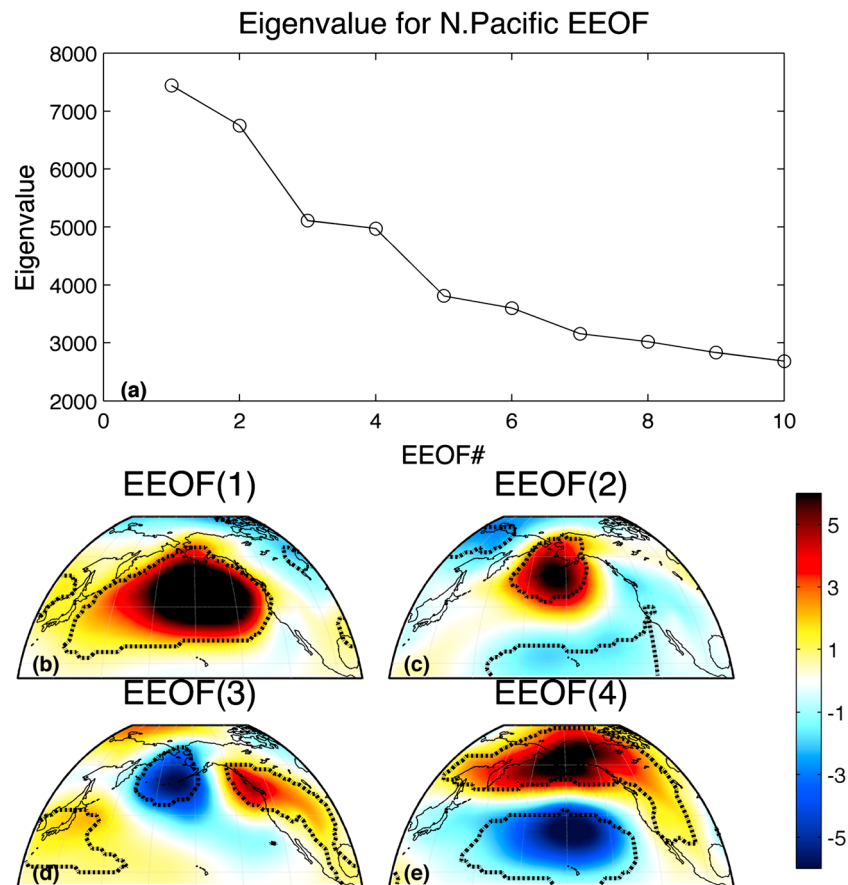


Figure 4. (a) The eigenvalues corresponding to the first 10 extended empirical orthogonal functions (EEOFs) of November–March $7\text{--}20\text{ year}^{-1}$ band-pass filtered 850 hPa geopotential height anomalies over the North Pacific ($15\text{--}80^{\circ}\text{N}$, $125^{\circ}\text{E}\text{--}90^{\circ}\text{W}$)—see text for details. (b–e) The central patterns for the first four EEOFs of November–March $7\text{--}20\text{ year}^{-1}$ band-pass filtered 850 hPa geopotential height anomalies. Anomaly values (m) are designated by the red/blue color bar at the right of the figure. The black contour designates the $p < 0.10$ value.

time series from the residual fields and the EEOF3 (EEOF4) time series from the full fields is $r = 0.93$. Hence, while the following discussion is based upon the EEOF analysis of the residual anomalies, the results are quantitatively similar to those obtained by using the second leading pair of EEOFs derived from the full fields.

To represent the time evolution of the pair of time-lagged modes, we use the time series for the leading mode (EEOF1) and refer to the standardized version as the PDP index (Figure 5a). Generally, we find that the index has enhanced variability from ~ 1900 to 1930 and from the mid-1980s onward, with more quiescent activity in the intervening period, in agreement with the time evolution the PDP index from the shorter duration NCEP/NCAR Reanalysis 1 data [Anderson *et al.*, 2016b]. The spatial evolution of the PDP itself then can be represented by the time-lagged maps that comprise the EEOF1 (Figures 5b–5g). As expected, we see that for lag = -2 years, a distinct meridional dipole in 850 hPa height anomalies is situated across the North Pacific (Figure 5b). Over the course of the next 2–3 years (Figures 5d and 5e), the southern lobe of the dipole progresses northeastward and establishes a zonal dipole with the eastern lobe situated off the coast of western North America and a corresponding pressure anomaly of opposite sign over the Bering Strait. Subsequently, the western lobe progresses southeastward to a location over the subtropical central North Pacific, while the eastern pole shifts northwestward to a location over the Aleutian islands, establishing a meridional dipole of opposite sign to the one preceding the PDP index (Figures 5f and 5g).

To confirm that this evolution is not simply an artifact of the use of the residual 850 hPa geopotential height anomalies, we regress the PDP index against time-lagged values of the interannual 850 hPa geopotential height anomalies (Figure 6). As with the time-lagged maps of the EEOF1, a distinct meridional dipole in

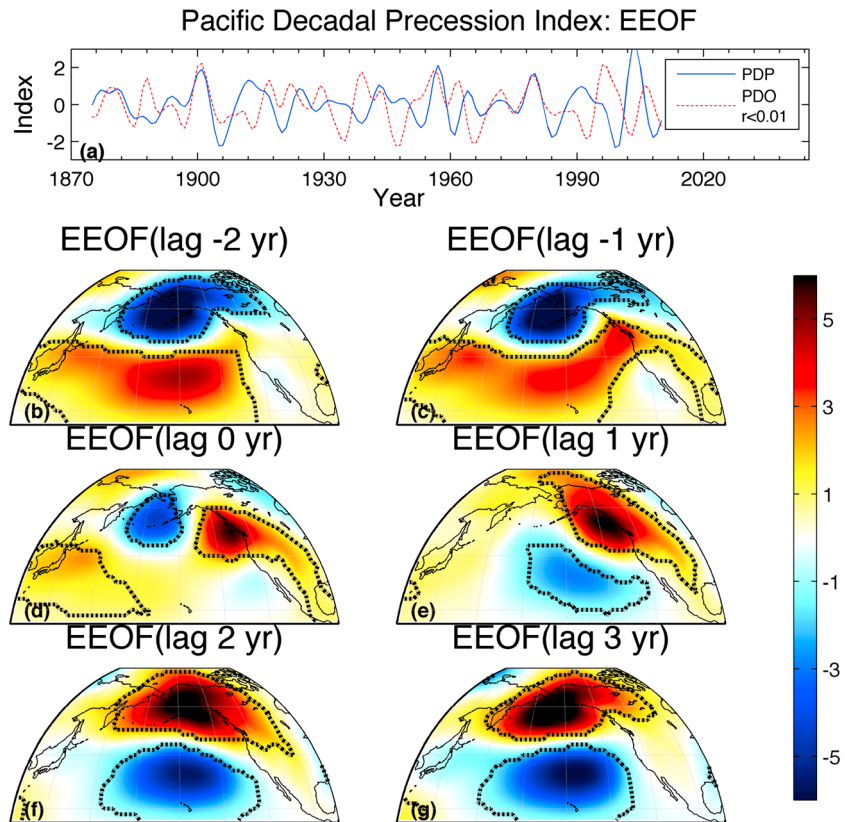


Figure 5. (a) The evolution of the Pacific Decadal Precession (PDP) index (blue line), defined as the normalized time series of the first Extended Empirical Orthogonal Function (EEOF) of November–March 7–20 year⁻¹ band-pass filtered residual 850 hPa geopotential height anomalies in the North Pacific (15–80°N, 125°E–90°W), after removing the first EOF of low-frequency pressure variations over the central North Pacific characteristic of the Pacific Decadal Oscillation (PDO)—see text for details. For comparison, the evolution of an independent PDO index—based upon NOAA’s Extended Reconstructed Sea Surface Temperature version 4 data with the same 7–20 year⁻¹ band-pass filter applied—is also shown (red line). (b–g) The multiple patterns of November–March 7–20 year⁻¹ band-pass filtered 850 hPa geopotential height anomalies comprising the first EEOF of the residual anomalies in the North Pacific (15–80°N, 125°E–90°W). Anomaly values (m) are designated by the red/blue color bar at the right of the figure. The black contour designates the $p < 0.10$ value. Positive (negative) years indicate that the pattern lags lead the PDP index time series shown in Figure 5a.

850 hPa height anomalies across the North Pacific emerges at lag = -3 years (Figure 6a) that subsequently rotates counterclockwise and establishes a zonal dipole concurrent with the index (Figure 6d). To further represent the full evolution of the North Pacific 850 hPa height anomalies, vis-à-vis those that accompany the PDP index, we establish a circular transect centered on the extratropical central North Pacific and use it to construct a Hovmöller diagram of the time evolution of the low-frequency 850 hPa geopotential height anomalies along the transect (Figure 6e). For comparison, we follow the lead of the MJO community [Kiladis et al., 2014] and construct a second Hovmöller diagram by using the spatiotemporal anomalies reconstructed from only the first two leading EEOF modes of lagged variability, which comprise the spatiotemporal evolution of the PDP within the 20Cv2 Reanalysis data.

As can be seen, there is substantial low-frequency variability across the entire transect at all times. However, there are also distinct periods in which the low-frequency variability shows organized movement along the transect, with a predominant sense of counterclockwise precession (although during certain periods, there is also an apparent clockwise progression, e.g., 1930–1950). Further, these periods of organized counterclockwise rotation along the transect align with the evolution of the PDP itself, although there are also periods of organized counterclockwise rotation along the transect that, while characteristic of the PDP, are not captured by the first two leading EEOF modes of lagged variability (e.g., ~1960–1970 and ~1985–1995), suggesting that, as with the MJO [Roundy and Schreck, 2009], the PDP may require the inclusion of additional modes of lagged variability to represent more nuanced features of its evolution.

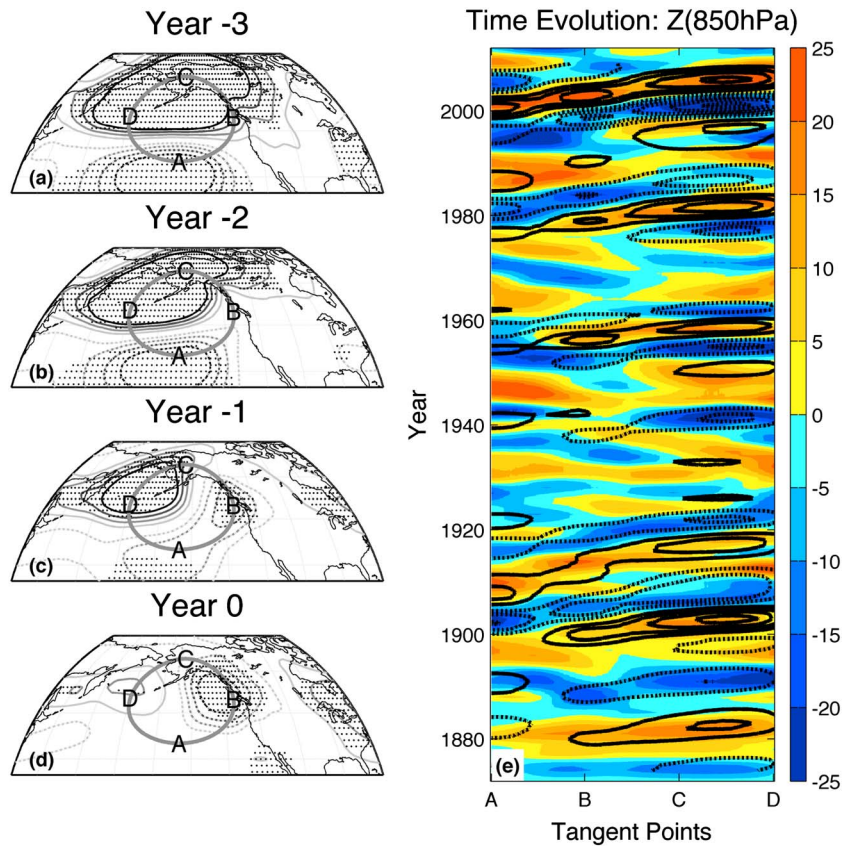


Figure 6. (a–d) Lag regression of November–March 850 hPa geopotential height anomalies onto the Pacific Decadal Precession (PDP) index, shown in Figure 5a. Positive (negative) values shown as solid (dashed) contours. Contour interval 1 m; the zero contour is omitted. Stippling indicates that regression coefficients exceeded the $p < 0.10$ value. Negative lags indicate that the atmospheric fields lead the PDP index. (e) Shading: Hovmöller diagram of 7–20 year⁻¹ band-pass filtered November–March 850 hPa geopotential height anomalies along the transect (i.e., grey arc) in Figures 6a–6d (x axis) plotted as a function of year (y axis). Anomaly values (m) are designated by the red/blue color bar at the right of the panel. Contours: Same as shading, except for 850 hPa geopotential height anomalies reconstructed by using the eigenvectors and eigenvalues for only the first two EEOFs of residual 850 hPa geopotential height anomalies in the North Pacific (15–80°N, 125°E–90°W)—see text for details. Positive (negative) values are shown as solid (dashed) contours. Contour interval is 5 m; the zero contour is omitted.

3.2. Real-Time Monitoring

The PDP index as developed and described in the previous section is not intended to serve as a real-time monitoring index but instead as a retrospective state estimator that can facilitate the analysis and diagnosis of the underlying phenomena and processes in a consistent framework. That said, as with the MJO, there is likely to be a need to track the state of the PDP in real time, particularly given the relation of the PDP to, e.g., extended droughts across California and the northwestern US, exceptional warmth in the Gulf of Alaska, and abnormally warm (cold) wintertime temperatures across the western U.S. (eastern North America) [Anderson et al., 2016a, 2016b]. As such, we describe here a method for doing so, based upon the (near) real-time data taken from the NCEP/NCAR Reanalysis 1.

We start by performing the exact same procedure as applied to the 20Cv2 data (see section 3.1). In particular, we construct the spatiotemporal matrix of 7–20 year⁻¹ band-pass filtered November–March 850 hPa geopotential height anomalies over the domain 15–80°N and 125°E–90°W. We then linearly remove via least squares regression signal related to the time series for the first EOF of the (nonextended) low-frequency pressure variations over the central North Pacific, which is characteristic of the PDO (not shown). Next we extend the spatiotemporal matrix of residual 850 hPa geopotential height anomalies by including (time) lagged values from 0 to 5 years at 1 year increments and calculate the EEOFs for this matrix. Again, the leading EEOF represents the PDP and the standardized version of its time series is the PDP index.

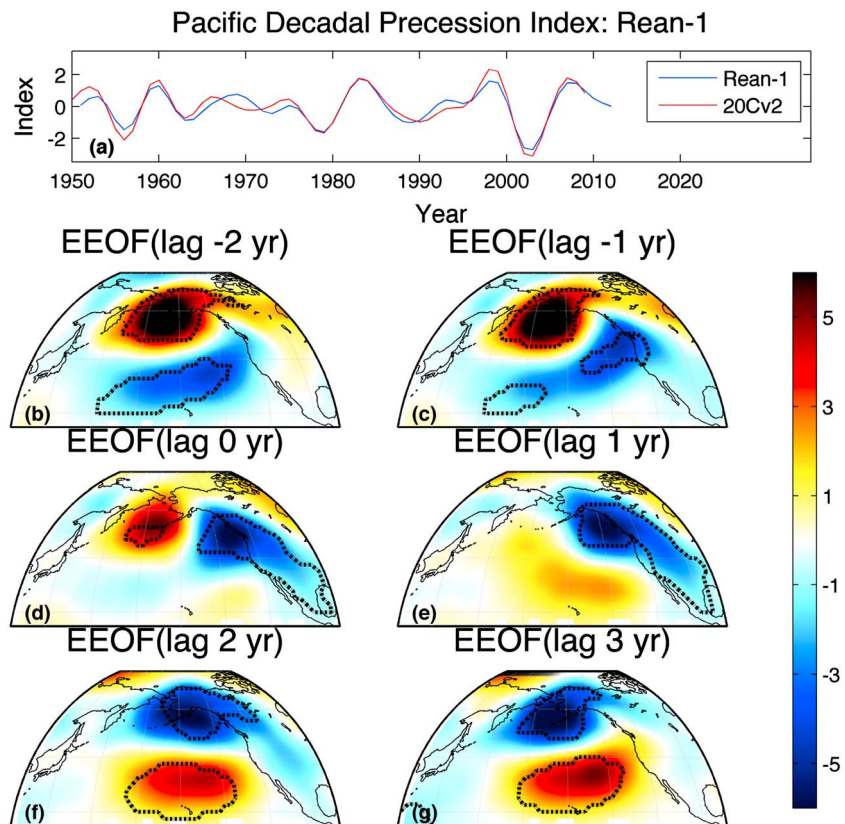


Figure 7. Same as Figure 5, except for the data taken from the NCEP/NCAR Reanalysis-1 data (R-1) for the period of 1948–2015. The red line is the same time series as in Figure 5a.

Not unexpectedly, the time evolution of the PDP as revealed in the R-1 data aligns well with that obtained from the longer, less-constrained 20Cv2 data (Figure 7a). Further, the spatial evolution of the PDP in the R-1 data shows the same sense of progression from a meridionally oriented dipole (Figure 7b) to a zonally oriented one (Figures 7c and 7d), back to a meridionally oriented dipole of opposite sign (Figures 7f and 7g) approximately 5 years later. However, the time series for the PDP based upon the extended covariance matrix is truncated in time and only can be used to provide a state estimate up through the extended winter of 2011–2012 (given the duration of the R-1 data used here).

To obtain a real-time estimate of the current state of the PDP, we again modify a technique taken from the MJO community [Kikuchi *et al.*, 2012]. In particular, the standard time series for a particular EEOF is given by the average projection of the full suite of EEOF maps (six in this case) onto the full anomaly field at the appropriate lead/lag time. We can obtain an *approximation* of this time series by performing the spatial regression of just the central EEOF map (the third map in our case) with the lag-0 anomaly field. Note that, while the spatial evolution of the PDP is lost when the lead/lag maps for a single EEOF are excluded, it can be reintroduced by performing the same analysis on the orthogonal, companion EEOF, in this case EEOF2. Figures 8a and 8b show the two central maps (EEOF1 and EEOF2) used to estimate the state of the zonal (EEOF1) and meridional (EEOF2) phases of the PDP. Figure 8c shows the historic evolution of the two EEOFs (derived from the full suite of EEOF maps) and the real-time estimate based only upon the central maps. As can be seen the real-time estimate approximates well the historic evolution during the period of overlap. However, when using only the central maps (along with the 0-lag anomaly field), it is possible to extend the time series across the full period of available data and capture the recent zonal phase of the PDP that has influenced much of the North Pacific/North American sector over the last few years [Anderson *et al.*, 2016b].

3.3. PDP in the CCSM4

We now apply our methodology for producing the PDP index (described in full in the previous section) to the preindustrial control simulation from the CCSM4, recognizing that an evaluation of the full suite of CMIP5

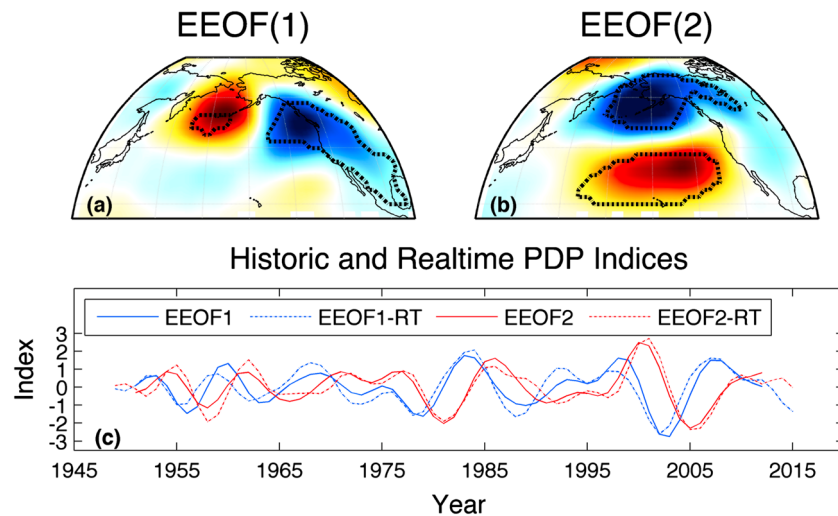


Figure 8. (a and b) The central patterns for the first two EEOFs of November–March 7–20 year⁻¹ band-pass filtered residual 850 hPa geopotential height anomalies in the North Pacific (15–80°N, 125°E–90°W), after removing the first EOF of low-frequency pressure variations over the central North Pacific characteristic of the Pacific Decadal Oscillation (PDO)—see text for details. Data taken from R-1 for the period of 1948–2015. Anomaly values (m) are designated by the same red/blue color bar as in Figure 7. The black contour designates the $p < 0.10$ value. (c) The historic (solid) and real-time (dashed) evolution of the first (blue) and second (red) EEOFs—see text for details.

models will be presented in a subsequent manuscript. Figure 9a shows the PDP index derived from the CCSM4. The model index has a modulated time evolution with periods of enhanced (e.g., years 160–200) and damped variability (e.g., years 450–400), as seen in the observations. However, unlike the observed PDP, the evolution of the spatial patterns corresponding to the “PDP” index in the CCSM4 depicts a standing, meridionally orientated dipole (Figures 9b–9g) only, with no analogue to the zonal dipole found in the observations. The same holds if the EEOF2 spatial patterns, as derived from the extended residual North Pacific 850 hPa geopotential height anomalies, are examined (not shown).

The lack of progression, or precession, of the dipole around the North Pacific basin is confirmed when looking at the lagged regression fields preceding, concurrent, and following the PDP time series (Figures 10a–10d). Unlike in the observations, the meridional dipole found in years $-2/-1/0$ is followed by a meridional dipole of opposite sign the following year (year 1) with no intervening zonal dipole phase. Similarly, the Hovmöller diagram for the spatiotemporal anomalies reconstructed from the first two leading EEOF modes of lagged variability shows no signal at the zonal nodes of the transect (B and D). The Hovmöller diagram of the time evolution of the full 850 hPa geopotential height anomalies along the transect does indicate low-frequency variations at these locations; however, unlike the observations, there is no tilt to the anomalies indicative of propagation of the anomalies along the transect (cf. Figure 6e). Instead, the anomalies tend to occur at all points on the transect concurrently and with the same sign. Indeed, anomalies at the zonal nodes correspond to the basin-wide evolution of a PDO-like monopole associated with EOF1 of the (nonextended) low-frequency pressure variations over the central North Pacific (not shown). Finally, as an aside, the magnitude of the anomalies along the transect, even for the full 850 hPa geopotential height fields, is larger than observed, suggesting that the atmospheric variability over the North Pacific of the CCSM4 in the 7–20 year⁻¹ band tends to be larger than observed. A full diagnosis of the source of this enhanced variability is beyond the scope of this paper.

4. Discussion

This study develops a framework to aid future analysis and diagnosis of the PDP’s characteristics and underlying processes so as to help advance our understanding of its evolution. Recognizing the complex nature of the coupled ocean-atmosphere climate system, we expect that progress toward this understanding will take substantial analysis using multiple lines of enquiry over many years. While plausible hypotheses for the PDP’s evolution have been discussed elsewhere [Anderson *et al.*, 2016a], Figure 11 briefly demonstrates the utility of the framework developed here which, through its application, provides another emergent

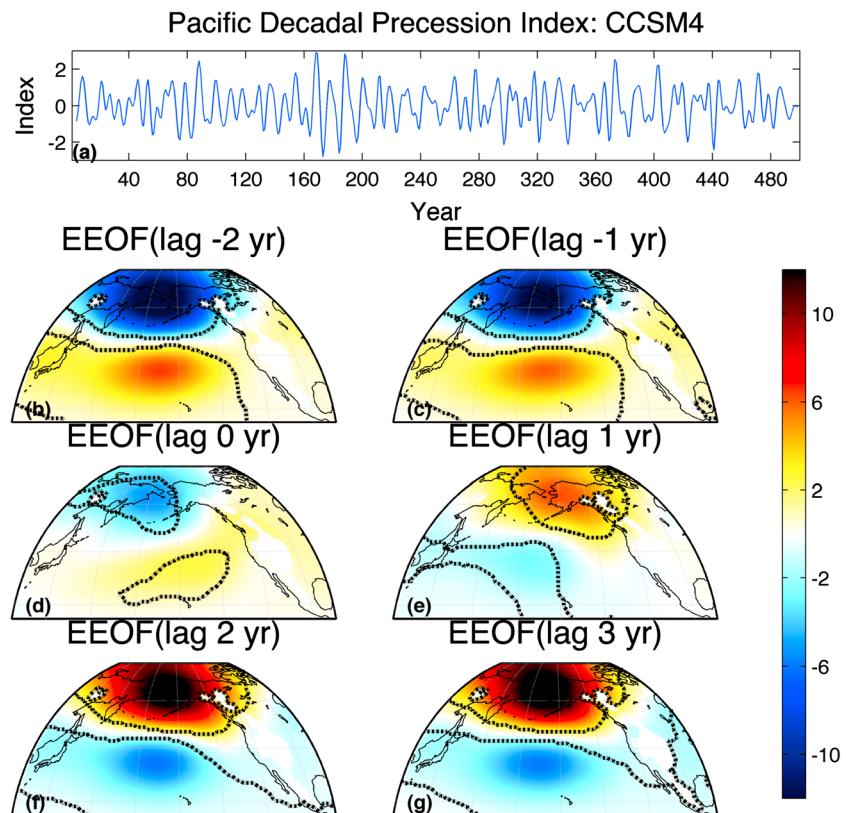


Figure 9. Same as Figure 5, except for the data taken from a 500 year control simulation of the Community Climate Simulation Model version 4 (CCSM4).

mechanism for future study. Here we take the observed PDP index derived in section 3.1 and regress it against time-lagged values of interannual surface and subsurface temperature anomalies (the latter of which is represented by the depth averaged 0–300 m temperature anomalies from the Simple Ocean Data Assimilation (SODA) forced by the 20CRv2 for the period of 1871–2011 [Carton and Giese, 2008]). We then take the CCSM4 PDP index derived in section 3.3 and regress it against time-lagged values of its interannual surface and subsurface temperature anomalies (the latter of which is represented by sea-surface height anomalies which, while not an exact analogue to the observed data, provide a proxy for the depth-averaged temperature anomalies).

As noted previously [Anderson *et al.*, 2016a, 2016b], during the north-south phase of the observed PDP, significant cooling of the surface waters presides over the western and central tropical Pacific and extends into the eastern Pacific and subpolar North Pacific, while warming spans the subtropical and extratropical North Pacific (year -2 in Figures 5 and 11); these anomalies subside as the PDP shifts into its east-west phase (year 0 in Figures 5 and 11) and subsequently remerge with opposite sign as the observed PDP re-establishes its north-south orientation (year 2 in Figures 5 and 11). Meanwhile, subsurface warming initially co-locates with surface temperature changes in the central North Pacific. As time progresses, however, the subsurface warming does not weaken but expands and shifts equatorward to the western tropical Pacific. The subsurface anomalies subsequently shift eastward into the central tropical Pacific at the same time that co-located surface temperature signatures re-emerge in this region.

Turning to the evolution of the “PDP” in the CCSM4 preindustrial run, initially, the surface and subsurface temperature signatures that accompany the north-south phase (year -2 in Figures 9 and 11) are similar to their observed counterparts. However, unlike in the observations, both the surface and subsurface signatures subside as the overlying atmospheric anomalies enter their transition stage. In turn no new anomalies develop during the latter stages of the PDP evolution, suggesting as before that, within the CCSM4, the “PDP” comprises a single (north-south) phase characteristic of the NPO, which is damped over time.

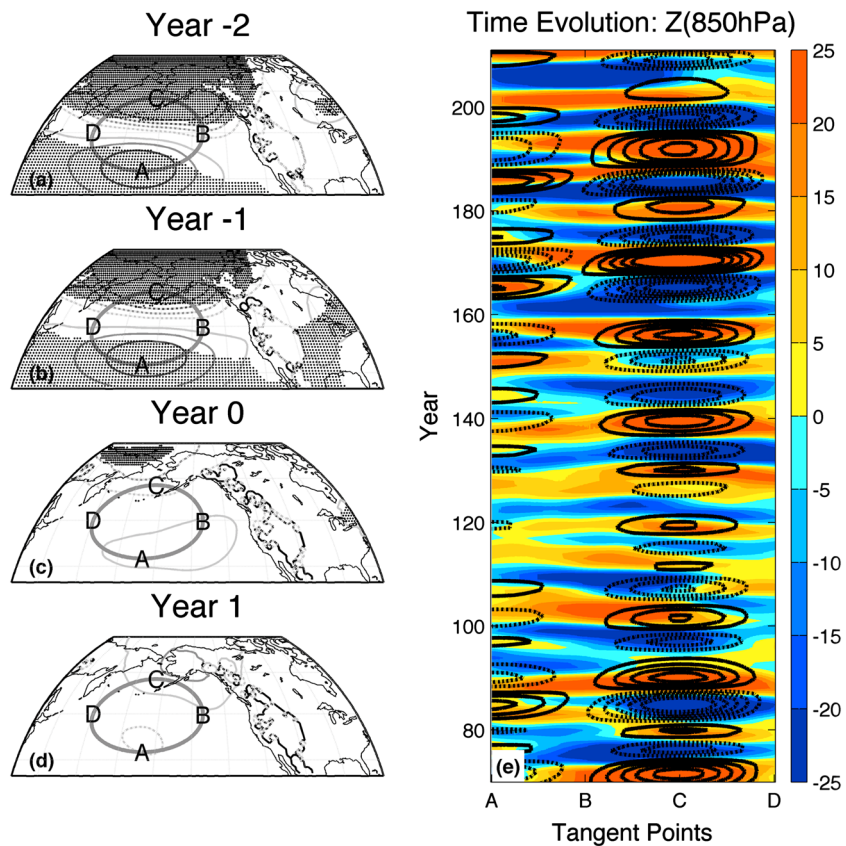


Figure 10. Same as Figure 6, except for the data taken from a 500 year control simulation of the CCSM4. (e) Only 140 years of the 500 year simulation are shown so as to better compare with the 140 year observational record (cf. Figure 6e).

Therefore, this analysis suggests that the oscillatory behavior of the observed PDP is sustained (in part) by extratropical subsurface temperature signatures that remerge in the central tropical Pacific 4–5 years later. By contrast, while the north-south phase of the PDP in the CCSM4 coincides with similar surface and subsurface temperature signatures as in the observations, the CCSM4 lacks the equatorward migration of subsurface temperature anomalies from the extratropics into the central tropical Pacific, leading to a decay of the simulated “PDP” pattern over time. That said, the processes underpinning the observed PDP’s full evolution still need to be elucidated since it is unclear from this analysis what mechanism sustains the east-west phase of the PDP—which is of similar magnitude as the north-south phase—given the absence of significant surface temperature signatures during this period of the PDP’s evolution.

5. Summary

In this paper, we developed a common method for tracking the Pacific Decadal Precession (PDP) and thus provide a consistent framework for future analysis and diagnosis of the characteristics, phenomena, and processes underlying the PDP. Our method—inspired by work to track the Madden-Julian Oscillation (MJO)—is based upon an extended EOF (EEOF) analysis of the quasi-decadal variations in lower tropospheric pressure patterns over the North Pacific during boreal winter. When applied to NOAA’s 20th Century Reanalysis version 2 (20Cv2), we capture the spatial progression of the PDP (Figure 5) similar to that revealed by lagged teleconnectivity of the North Pacific pressure fields (Figures 1 and 3) and can consequently estimate the state of the PDP in the past. In addition, as with the MJO, the method can be used to reconstruct the “PDP-filtered” evolution of the historical pressure patterns over the North Pacific.

While the method developed here provides a “best estimate” of the historical state of the PDP, it cannot provide a real-time estimate of that state. Through use of the spatial patterns from the EEOF analysis, however, we develop an alternate method for tracking the PDP. This new method recovers the evolution of both

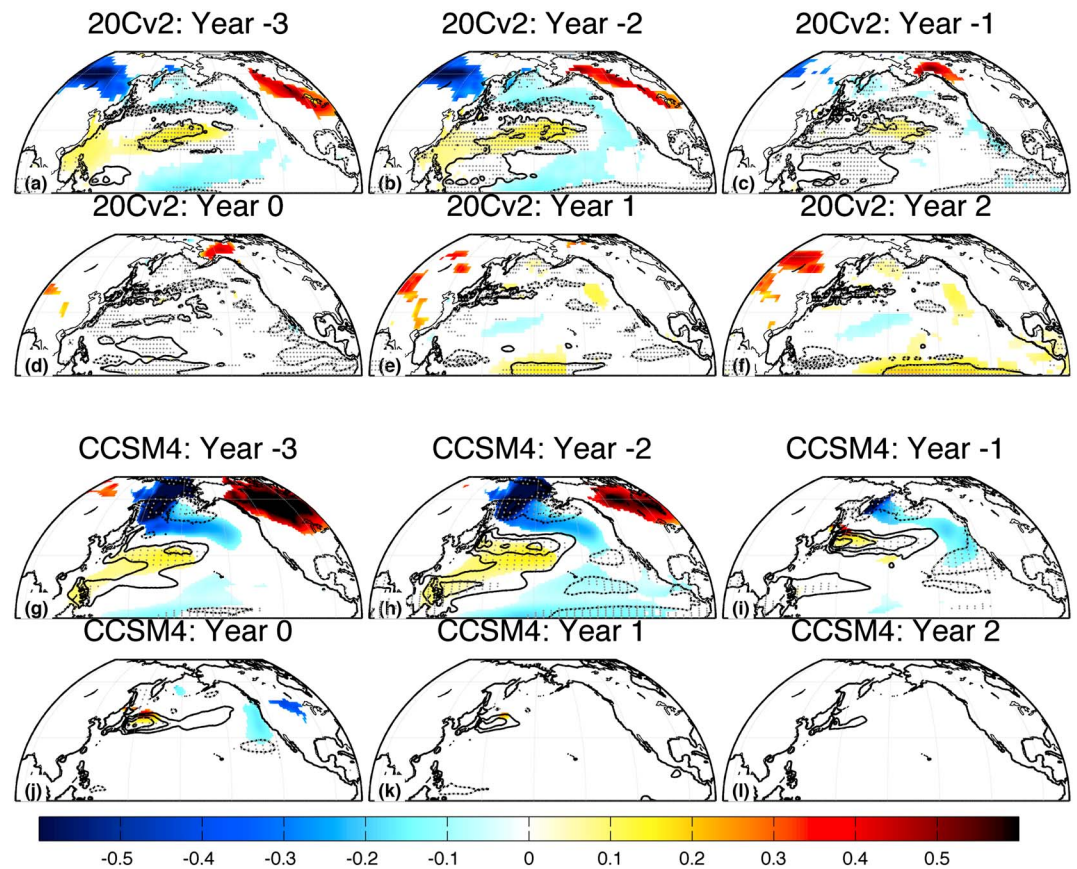


Figure 11. (a–f) Shading: lag/lead regression of November–March surface temperature anomalies onto the observed Pacific Decadal Precession (PDP) index, shown in Figure 5a. Anomalies (K) are designated by the red/blue color bar at the bottom of the figure. Only values significant at the $p < 0.10$ threshold are shown. Contours: lag/lead regression of November–March 0–300 m depth averaged temperature anomalies onto the PDP index; data are taken from the concurrent SODAsi.2 forced by 20CRv2. Positive (negative) values are shown as solid (dashed) contours. Contour interval 0.1 K; the zero contour is omitted. Stippling indicates that regression coefficients exceed the $p < 0.10$ value. Positive (negative) years indicate that the pattern lags (leads) the PDP index time series. (g–l) Same as Figures 11a–11f, except for the CCSM4 anomalies as regressed against the simulated PDP index, shown in Figure 9a. Here sea-surface height anomalies are used as a proxy for depth averaged temperature anomalies. Contour interval 5 mm; the zero contour is omitted. Stippling indicates that regression coefficients exceed the $p < 0.10$ value.

phases of the PDP through the second half of the 20th century and the early 21st century (Figure 7) and also provides an estimate of the state of both phases through the (near) present, which allows for more robust monitoring of the PDP (Figure 8). This real-time monitoring can prove important as the potential downstream impacts of the PDP (e.g., drought/pluvial periods in the Western U.S., propensity for more frequent cold and heat waves over the central and eastern U.S. and Canada, and warming and cooling of waters over the eastern North Pacific) may have important decadal signals that pose socioeconomic concerns. While real-time assessment of the contribution of the PDP to specific decadal signals and their impacts is a topic for future research, the ability to track and detect the state of the North Pacific atmosphere will nevertheless prove vital for seasonal and interannual climate studies.

Finally, as a proof of concept, we apply the method to a 500 year preindustrial control simulation of the Community Climate System Model version 4 (CCSM4). While the method identifies quasi-decadal variations in meridional dipole pressure anomalies over the North Pacific, the characteristics of their spatial evolution do not match that found in the observations (Figure 9). Indeed, within the CCSM4, there is no sense of precession of the dipole anomalies as in the observations; instead, the quasi-decadal variations are more characteristic of a standing wave-like feature. Two conclusions can be drawn from this analysis. First, the lack of a PDP-like mode of variability in CCSM4 indicates that the method developed here for tracking the PDP via use of

band-pass filtered data in combination with EEOF analysis does not artificially introduce precession of pressure patterns as revealed in the observational data. Second, it indicates that, much like the MJO, current versions of numerical coupled ocean-atmosphere models may fail to adequately represent the spatial and temporal evolutions of an observed mode of variability. This may be particularly true for patterns of Pacific decadal variability (PDV) and the CCSM4 in particular. For example, *Deser et al.* [2014] found that, while the CCSM4 has realistic temporal and even spatial reproductions of PDV, the simulated link between the tropical Pacific and PDV is weaker than observed. Should the evolution of the central tropical Pacific signature (Figures 11a–11f) indeed be important for exciting and maintaining the PDP, the lack of this feature in the CCSM4 could explain the model's lack of "precession." Future analyses of this mode of variability, in both observed and simulated data, may in turn help inform improvements to the physics and dynamics of these models, much as they have through comparative analyses of the MJO within and across various data sets.

Acknowledgments

This work was supported by the National Science Foundation (AGS-0958907) and the Department of Energy (DE-SC0006914—B.T.A. and G.D.S.). E.D. was supported by the National Science Foundation (OCE-1356924 and OCE-1419292). All data for this paper are properly cited and referred to in the reference list.

References

- Anderson, B. T., D. J. S. Gianotti, G. Salvucci, and J. Furtado (2016a), Dominant timescales of potentially predictable precipitation variations across the continental United States, *J. Clim.*, *29*, 8881–8897, doi:10.1175/JCLI-D-15-0635.1.
- Anderson, B. T., D. J. S. Gianotti, J. Furtado, and E. Di Lorenzo (2016b), A decadal precession of atmospheric pressures over the North Pacific, *Geophys. Res. Lett.*, *43*, 3921–3927, doi:10.1002/2016GL068206.
- Benmarhnia, T., M.-F. Sottile, C. Plante, A. Brand, B. Casati, M. Fournier, and A. Smargiassi (2014), Variability in temperature-related mortality projections under climate change, *Environ. Health Perspect.*, *122*, 1293–1298.
- Carton, J. A., and B. S. Giese (2008), A reanalysis of ocean climate using Simple Ocean Data Assimilation (SODA), *Mon. Weather Rev.*, *136*, 2999–3017.
- Compo, G. P., et al. (2011), The Twentieth Century Reanalysis Project, *Q. J. R. Meteorol. Soc.*, *137*, 1–28.
- Dell, M., B. F. Jones, and B. A. Olken (2008), Climate change and economic growth: Evidence from the last half century NBER Working Paper No. 14132.
- Deser, C., et al. (2014), ENSO and Pacific Decadal Variability in the Community Climate System Model version 4, *J. Clim.*, *25*, 2622–2651.
- Di Lorenzo, E., et al. (2008), North Pacific Gyre Oscillation links ocean climate and ecosystem change, *Geophys. Res. Lett.*, *35*, L08607, doi:10.1029/2007GL032838.
- Doney, S. C., et al. (2012), Climate change impacts on marine ecosystems, *Annu. Rev. Mar. Sci.*, *4*, 11–37.
- Enfield, D. B., A. M. Mestas-Núñez, and P. J. Trimble (2001), The Atlantic Multidecadal Oscillation and its relation to rainfall and river flows in the continental U.S., *Geophys. Res. Lett.*, *28*, 2077–2080, doi:10.1029/2000GL012745.
- Gent, P. R., et al. (2011), The Community Climate System Model version 4, *J. Clim.*, *24*, 4973–4991.
- Gosling, S. N., J. A. Lowe, G. R. McGregor, M. Pelling, and B. D. Malamud (2009), Associations between elevated atmospheric temperature and human mortality: A critical review of the literature, *Clim. Change*, *92*, 299–341.
- Kalnay, E., et al. (1996), The NCEP/NCAR 40-year reanalysis project, *Bull. Am. Meteorol. Soc.*, *77*(3), 437–470.
- Kikuchi, K., B. Wang, and Y. Kajikawa (2012), Bimodal representation of the tropical intraseasonal oscillation, *Clim. Dyn.*, *38*, 1989–2000, doi:10.1007/s00382-011-1159-1.
- Kiladis, G. N., J. Dias, K. H. Straub, M. C. Wheeler, S. N. Tulich, K. Kikuchi, K. M. Weickmann, and M. J. Ventrice (2014), A comparison of OLR and circulation-based indices for tracking the MJO, *Mon. Weather Rev.*, *142*, 1697–1715.
- Linkin, M. E., and S. Nigam (2008), The North Pacific Oscillation–West Pacific teleconnection pattern: Mature-phase structure and winter impacts, *J. Clim.*, *21*, 1979–1997.
- Madden, R., and P. Julian (1971), Detection of a 40–50 day oscillation in the zonal wind in the tropical Pacific, *J. Atmos. Sci.*, *28*, 702–708.
- Mantua, N. J., S. R. Hare, Y. Zhang, J. M. Wallace, and R. C. Francis (1997), A Pacific interdecadal climate oscillation with impacts on salmon production, *Bull. Am. Meteorol. Soc.*, *78*(6), 1069–1079.
- Mendelsohn, R. O., and A. Dinar (2009), *Climate Change and Agriculture: An Economic Analysis of Global Impacts, Adaptation and Distributional Effects*, Edward Elgar, Cheltenham, U. K.
- Moritz, C., and R. Agudo (2013), The future of species under climate change: Resilience or decline?, *Science*, *341*, 504–508.
- Nigam, S., and S. Baxter (2015), Teleconnections, in *Encyclopedia of Atmospheric Sciences*, 2nd ed., vol. 3, edited by G. R. North, J. Pyle, and F. Zhang, pp. 90–109, Academic Press, Cambridge, Mass.
- Roundy, P. E., and C. J. Schreck (2009), A combined wave-number-frequency and time-extended EOF approach for tracking the progress of modes of large-scale organized tropical convection, *Q. J. R. Meteorol. Soc.*, *135*, 161–173.
- Schlenker, W., D. Lobell, and J. Costa-Roberts (2011), Trends and global crop production since 1980, *Science*, *333*, 616–620.
- Solomon, A., et al. (2011), Distinguishing the roles of natural and anthropogenically forced decadal climate variability, *Bull. Am. Meteorol. Soc.*, *92*, 141–156.
- Taylor, K. E., R. J. Stouffer, and G. A. Meehl (2012), An overview of CMIP5 and the experiment design, *Bull. Am. Meteorol. Soc.*, *93*, 485–498.
- Walker, G. T., and E. W. Bliss (1932), World weather V, *Mem. R. Meteorol. Soc.*, *4*, 53–83.
- Wallace, J. M., and D. S. Gutzler (1981), Teleconnections in the geopotential height field during the northern hemisphere winter, *Mon. Weather Rev.*, *109*, 784–812.
- Walther, G.-E., et al. (2002), Ecological responses to recent climate change, *Nature*, *416*, 389–395.
- Wang, S.-Y., R. R. Gillies, J. Jin, and L. E. Hipps (2009), Recent rainfall cycle in the Intermountain Region as a quadrature amplitude modulation from the Pacific Decadal Oscillation, *Geophys. Res. Lett.*, *36*, L02705, doi:10.1029/2008GL036329.
- Weare, B. C., and J. S. Nasstrom (1982), Examples of extended empirical orthogonal function analysis, *Mon. Weather Rev.*, *90*, 481–485.
- Zhang, C. (2005), Madden-Julian Oscillation, *Rev. Geophys.*, *43*, RG2003, doi:10.1190/1.1988182.